





# Unravelling the corrosion processes at steel/bentonite interfaces in in situ tests

Paul Wersin<sup>1</sup>  | Jebril Hadi<sup>1</sup> | Mirjam Kiczka<sup>1</sup> | Andreas Jenni<sup>1</sup> | Jean-Marc Grenèche<sup>2</sup> | Nikitas Diomidis<sup>3</sup>  | Olivier X. Leupin<sup>3</sup> | Daniel Svensson<sup>4</sup> | Patrik Sellin<sup>4</sup> | Bharti Reddy<sup>5</sup>  | Nicholas Smart<sup>5</sup>  | Zhidong Zhang<sup>6</sup>

<sup>1</sup>Rock–Water Interaction, Institute of Geological Sciences, University of Bern, Bern, Switzerland

<sup>2</sup>Institut des Molécules et Matériaux du Mans (IMMM) UMR CNRS 6283, Le Mans Université, Le Mans, France

<sup>3</sup>National Cooperative for the Disposal of Radioactive Waste, Wettingen, Switzerland

<sup>4</sup>Swedish Nuclear Fuel and Waste Management Co., Solna, Sweden

<sup>5</sup>Jacobs, HQ Building, Thomson Avenue, Harwell Campus, Oxfordshire, UK

<sup>6</sup>Institute for Building Materials, ETH Zurich, Zurich, Switzerland

## Correspondence

Paul Wersin, Institute of Geological Sciences, University of Bern, 3012 Bern, Switzerland.

Email: [paul.wersin@geo.unibe.ch](mailto:paul.wersin@geo.unibe.ch)

## Funding information

Svensk Kärnbränslehantering; Nationale Genossenschaft für die Lagerung radioaktiver Abfälle

## Abstract

Microscopic and spectroscopic analyses were conducted on steel/bentonite interface samples removed from four in situ experiments that were carried out in three underground research laboratories at different temperatures and under different hydraulic and geochemical conditions. The results provide valuable information about the corrosion processes occurring in high-level radioactive waste repositories. Systematic patterns can be deduced from the results, irrespective of carbon steel grade, type of bentonite and its degree of compaction, geochemical environment or experimental setup. Thus, a clear dependence of the corrosion rates on temperature and exposure period, as well as on the availability of H<sub>2</sub>O and O<sub>2</sub> provided by the surrounding bentonite buffer, is observed. Furthermore, Fe(II) ions released by corrosion interact with the structural Fe in the clay. Recent developments highlight the usefulness of reactive transport modelling in understanding the coupled corrosion and Fe–clay interaction processes.

## KEYWORDS

bentonite, corrosion, in situ, iron, nuclear, reactive transport, steel, waste

## 1 | INTRODUCTION

The safety of high-level nuclear waste repositories is based on the multibarrier concept, which includes an engineered barrier system (EBS) (usually a metal waste-containing canister overpack surrounded by a backfill material such as bentonite) placed in a host rock located at depths of several 100 m below the

surface.<sup>[1]</sup> Iron-based alloys are foreseen as the canister materials of choice in a number of countries, for example, low carbon steel in France,<sup>[2]</sup> Switzerland<sup>[3]</sup> and the Czech Republic,<sup>[4]</sup> or cast iron inserts are also used for containing spent fuel assemblies inside a copper shell, such as in Sweden<sup>[5]</sup> and Finland.<sup>[6]</sup> This paper is focussed on the use of carbon steel canisters in a bentonite backfill.

This is an open access article under the terms of the Creative Commons Attribution-NonCommercial-NoDerivs License, which permits use and distribution in any medium, provided the original work is properly cited, the use is non-commercial and no modifications or adaptations are made.

© 2023 The Authors. *Materials and Corrosion* published by Wiley-VCH GmbH.

After repository closure, corrosion of steel canisters initially occurs under oxic conditions. The oxygen originates mainly from the partially saturated pore space of the emplaced bentonite. Upon depletion of oxygen, reducing conditions govern the corrosion process.<sup>[7,8]</sup> Moreover, the corrosion process will be influenced by the interaction of oxidised iron species with the bentonite clay, as shown by the longer time needed to reach steady-state conditions in the presence of bentonite.<sup>[9]</sup> These iron species can interact with the clay by sorption,<sup>[10]</sup> precipitation,<sup>[11]</sup> and complex redox processes.<sup>[12,13]</sup> In turn, corrosion and the Fe–clay interactions can affect the sealing properties of the bentonite barrier, such as its swelling capacity or hydraulic conductivity.<sup>[11,14]</sup> During the early stages of the repository operation, the EBS will be exposed to the heat emanating from the decaying radioactive waste inside the steel canisters.

Most experimental studies dedicated to steel corrosion in bentonitic environments have been performed in simplified model systems (Wersin et al.<sup>[14]</sup>, Diomidis and King<sup>[15]</sup> and references therein). Less work has focussed on conditions that are more representative of the repository, namely, low liquid/solid ratios and low Fe/bentonite ratios, variable redox conditions, higher temperatures, realistic dimensions, exposure to real microbial populations and longer timescales.

In situ experiments carried out in underground research laboratories (URLs) provide a good opportunity to study corrosion and Fe–bentonite interactions in environments representative of the early stages of the repository lifetime.<sup>[15]</sup> Here, we discuss and compare four in situ experiments carried out in three URLs with different types of steel and bentonite as well as in different geological and geochemical environments. These studies required careful analysis of the steel/bentonite interface after termination and dismantling of the in situ tests.

## 2 | MATERIALS AND METHODS

### 2.1 | Description of in situ tests

This section describes the four in situ experiments that are considered in this paper, as follows.

**ABM1 experiment:** The ABM test is an internationally supported in situ experiment conducted by SKB (Swedish Nuclear Fuel and Waste Management Co.) in crystalline rock in the Äspö Hard Rock Laboratory, Sweden. Within the ABM test, three test packages (ABM1, ABM2 and ABM3), consisting of various bentonite materials stacked on top of each other as blocks, were emplaced in three boreholes and heated by a central steel tube composed of

a common carbon steel, P235TR1.<sup>[16]</sup> The ABM1 experiment was conducted for a period of 2.4 years during which time the materials were exposed to elevated temperatures (above 100°C) and saturated simultaneously with artificial Äspö groundwater. After dismantling, a number of samples were taken, including the steel–bentonite interface zone from Block no. 3, which consisted of granular MX-80 that had been inserted inside a steel cage and exposed to a maximum temperature of 115°C. The experiment is described in detail in Svensson et al.<sup>[17]</sup> The analysis of the Fe–bentonite interface is documented in Wersin et al.<sup>[18]</sup>

**ABM2 experiment:** This experiment, which employed the same setup as ABM1, was conducted over a longer time period of 5.5 years with a maximum temperature of 130°C. After saturation with artificial groundwater for 1 year, heating was initiated. The cooling phase also lasted for about 1 year. The experiment is outlined in detail in Kaufhold et al.<sup>[19]</sup> and Hadi et al.<sup>[20]</sup> The analysis of the steel–bentonite interfaces is described in detail by Wersin et al.<sup>[21]</sup> It included 11 interface samples from 8 blocks, with 7 different bentonite materials: MX-80 from Wyoming (as the “caged” granular material in two different blocks), MX-80/quartz mixture (70:30) (as the “caged” granular material), Ibecoseal from Georgia, Ikosorb from Morocco, Kunigel VI from Japan, Rokle from the Czech Republic and Deponit CAN from Milos, Greece.

**FEBEX experiment:** The long-term full-scale engineered barrier experiment (FEBEX) in situ test was designed by ENRESA (the Spanish radioactive waste management organisation) and consisted of two steel heaters inside a perforated steel cylinder (15Mo3) surrounded by Ca–Mg bentonite (so-called FEBEX bentonite) inside a horizontal tunnel drilled into the crystalline rock at the Grimsel Test site, Switzerland. The bentonite blocks were exposed to natural saturation from the rock (primarily via a fracture zone) and heated to a maximum temperature of 100°C, leading to varying saturated conditions and temperatures during the test. Moreover, analysis of the monitoring and *post-mortem* data suggested that ingress of air occurred during the experiment, leading to spatially and temporally variable redox conditions.<sup>[22,23]</sup> After 5 years, the sections of the first heater were dismantled and replaced by a cement plug and a “dummy” cell after which heating of the second heater resumed. After the final termination and dismantling of the test after 18 years of exposure, a comprehensive *post-mortem* analysis was conducted.<sup>[24]</sup> This analysis also included the investigation of two steel/bentonite interface samples located between the “dummy” cell and the second heater (Section 62) and exposed to maximum temperatures of about 70°C. The first sample from block BM-B-41-1 macroscopically

showed a large interaction zone extending into the clay. In contrast, the second sample from block BM-B-41-2 showed no interaction zone at all, which was confirmed by scanning electron microscopy coupled with electron dispersive X-ray analysis (SEM/EDX). This study is described in detail in Hadi et al.<sup>[25]</sup>

*IC-A experiment:* This experiment consisted of pre-fabricated modules of unwelded and welded carbon steel coupons (ASTM A694-08 F65 and 516Gr 70) embedded in MX-80 bentonite (fabricated from both blocks and pellets) at different target dry densities (1450 and 1550 kg m<sup>-3</sup>) inside a stainless steel cylinder. The modules were manufactured and transported under anoxic conditions and emplaced in a vertical borehole in Opalinus Clay (an over-consolidated clayrock) in the Mont Terri URL and subsequently saturated naturally with Opalinus Clay porewater. The temperature around the borehole is ~14°C. The in situ experiment, which was initiated in 2012, is still in operation. Two of the modules were dismantled after 20 and 33 months, for analysis of the test coupons and the surrounding clay. Experimental details of the materials and procedures are outlined in Smart et al.<sup>[26]</sup> and Reddy et al.<sup>[27]</sup>

It should be pointed out that the IC-A experiment was specifically designed for studying corrosion processes, whereas the other in situ experiments described here were originally designed to study potential changes in bentonite.

## 2.2 | Analytical procedures

Two distinct analytical methodologies by two research teams were applied for the ABM1, ABM2 and FEBEX experiments on the one hand and the IC-A experiment on the other hand, as follows.

*ABM1, ABM2, FEBEX:* The analysis of the Fe/clay interfaces was based on a multimethod approach developed over the last few years and described in detail in Wersin and colleagues.<sup>[18,20,21]</sup> Two types of interface samples were prepared. The first type was utilised for microscopic analysis at high spatial resolution using SEM/EDX and  $\mu$ -Raman spectroscopy. To this end, interface samples were prepared by cutting, freeze-drying, resin impregnation and polishing. The second type included powdered “bulk” samples (slices taken parallel to the steel/clay contact were prepared and stored under anoxic conditions) for iron speciation by <sup>57</sup>Fe Mössbauer spectrometry, mineralogical analysis by X-ray diffraction (XRD) and elemental composition analysis by X-ray fluorescence (XRF). Using the XRF data for calibration, the elemental compositions obtained from SEM/EDX mapping could be quantified. This also

enabled an approximate estimate of the corrosion depth ( $d_{\text{corr}}$ ) to be made, considering the cylindrical geometry according to Wersin et al.<sup>[18]</sup>:

$$d_{\text{corr}} = d_{\text{CL}} \frac{V_{m(\text{Fe})}}{V_{m(\text{FeOOH})}} + \frac{1}{\rho_{\text{Fe}} A_s} \sum_{n=1}^z (r_n^2 - r_{n-1}^2) \pi h \rho_b f_c ([\text{Fe}]_n - [\text{Fe}]_c), \quad (1)$$

where  $d_{\text{CL}}$  ( $m$ ) is the corrosion layer (CL) thickness (measured microscopically),  $V_{m(\text{Fe})}$  and  $V_{m(\text{FeOOH})}$  are the molar volumes (m<sup>3</sup>/mol) of steel and goethite (the main corrosion product), respectively,  $\rho_{\text{Fe}}$  and  $\rho_b$  (kg/m<sup>3</sup>) are the density of steel and bentonite, respectively,  $A_s$  (m<sup>2</sup>) is the unit surface of the Fe source (the cylindrical steel surface),  $n$  is the number of areas in which the concentration of Fe is increased, corresponding to the measured Fe and background Fe mass fractions  $[\text{Fe}]_n$  and  $[\text{Fe}]_c$  (kg<sub>Fe</sub>/kg<sub>bent</sub>), respectively,  $r_n$  ( $m$ ) is the radius of the circle including the radius of the Fe source ( $r_o$ ) and the distance from the source to the area  $n$ ,  $z$  is the number of areas in which Fe is increased with respect to the pristine bentonite,  $f_c$  is the calibration factor for converting the Fe measured with EDX to the “true” concentration and  $h$  ( $m$ ) is the unit height of the cylinder.

*IC-A experiment:* The experimental and analytical details are described in Smart et al.<sup>[26]</sup> and Reddy et al.<sup>[27]</sup> The analysis of the corrosion coupons included weight loss measurements according to standard practices<sup>[28]</sup> to determine average corrosion rates. The CL was analysed with SEM/EDX and Raman spectroscopy and, for selected samples, the chemical composition of the CL was analysed by X-ray photoelectron spectroscopy.

The clay adjacent to the corrosion coupons was analysed by SEM/EDX and electron probe microanalysis on polished thin sections. The mineralogical composition of powdered samples was analysed by XRD. Other investigations included porewater and microbiological analyses (not reported here).

## 3 | RESULTS

### 3.1 | Metal side

The metal surface of all samples was covered by a CL consisting predominantly of various iron (oxyhydr)oxides (referred to as iron oxides in the following) (Table 1). In addition, siderite was identified in the ABM1, ABM2 and FEBEX experiments, while analyses suggested the presence of traces of an iron–sulphur compound in the IC-A experiment. It should be noted that due to technical

TABLE 1 Conditions and results of corrosion layer analysis from the in situ steel/bentonite interface samples.

Exp.	Max. temperature (°C)	Duration (year)	Corrosion products	Redox conditions	Avg. corr. rate corr. layer ( $\mu\text{m/a}$ )	Ref.
IC-A	14	1.7	mag, hem	"Anaerobic"	1.4–3.4 <sup>a</sup>	[26]
	14	2.8	mag, hem, Fe-S	"Anaerobic"	0.9–2.1 <sup>a</sup>	[27]
FEBEX	70	18	goe, hem, mag, sid, lep, mah	Mixed	6–11 <sup>b</sup>	[25]
ABM1	115	2.4	mag, hem, sid, goe, lep	Mixed	5–8 <sup>b</sup>	[18]
ABM2	130	5.5	mag, sid	Mixed	n.d.	[19–21]

Note: Blue font: Fe(III) oxides; green font: Fe(II) bearing corrosion products.

Abbreviations: Fe-S, (unidentified) FeS compound; goe, goethite; hem, haematite; lep, lepidocrocite; mag, magnetite; mah, maghemite; ma., maximum; n.d., not determined; sid, siderite.

<sup>a</sup>Determined from weight loss measurements.

<sup>b</sup>Estimated according to first term in Equation (1).

limitations in sample preparation, the metal could in many cases not be sampled together with the contacting clay. A prominent exception is the ABM1 sample, where the steel/bentonite interface remained intact during sample preparation and this enabled detailed probing of the CL in contact with the clay, although a small gap had formed during freeze-drying. An SEM micrograph of this sample (Figure 1a) shows that the CL consisted of an irregular mixture of lighter and darker aggregates (reflecting the iron-rich and clay-rich areas), respectively. An example of the  $\mu$ -Raman spectrum for the CL indicates the presence of magnetite and siderite (Figure 1b).

Corrosion products that are characteristic of both oxic and anoxic conditions were formed, containing both Fe(II) and Fe(III) ions. This indicates variable redox conditions in the experiments (Table 1). This was even the case for the IC-A experiment, in which great care was taken to prepare and partially presaturate the bentonite modules under anoxic conditions. The main corrosion product in that experiment was magnetite with only minor amounts of haematite present. In the case of the other experiments, the bentonite blocks were partially saturated after emplacement and the environment was initially oxidising. Thus, aerobic corrosion was active during the first stages, but it was eventually followed by anaerobic corrosion in these experiments as indicated by the presence of Fe(II)-bearing corrosion products.

From weight-loss measurements, the average corrosion rates could be accurately derived in the IC-A experiment, yielding rather low values of approximately 1–3  $\mu\text{m/a}$  (Table 1), which agree with the majority of the literature data on the anaerobic corrosion rate of iron.<sup>[29]</sup> A closer examination of these corrosion rates indicates a decrease with time for all the bentonite densities tested (Figure 2). In addition, the coupons

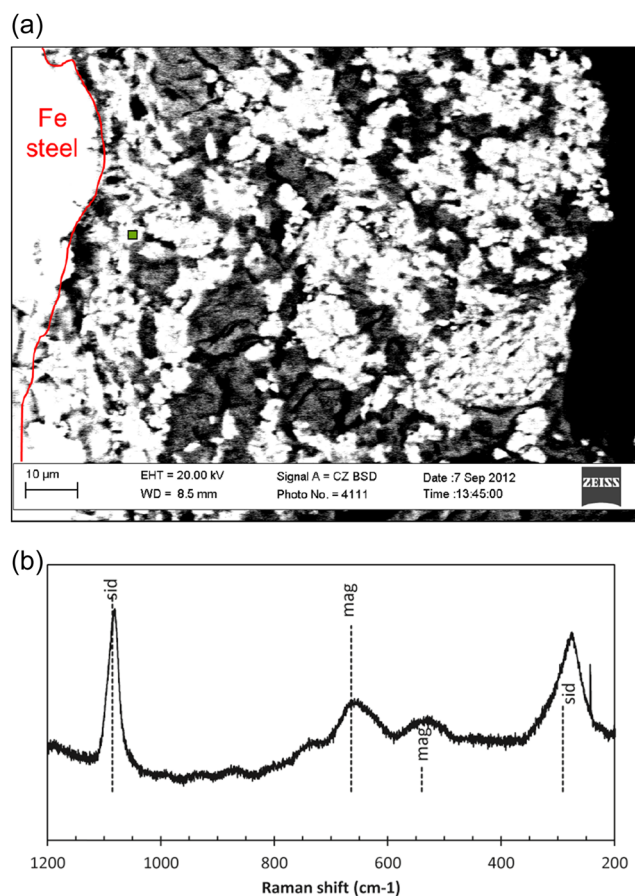
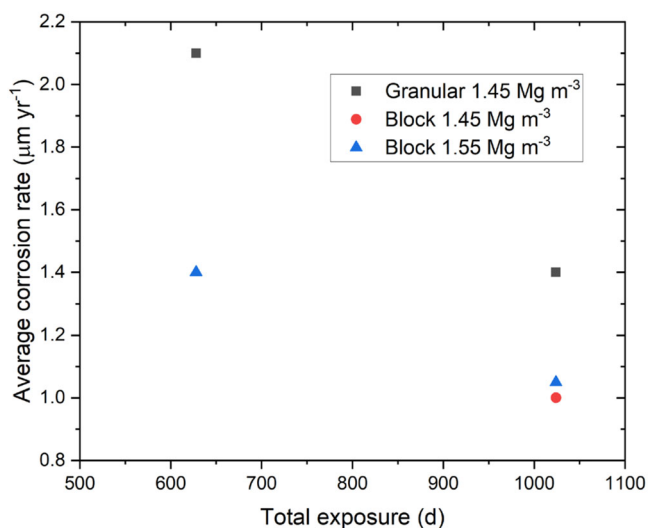


FIGURE 1 SEM (a) and  $\mu$ -Raman spectroscopic (b) analysis of the corrosion layer on the ABM1 sample: The upper back-scattered electron-SEM image shows a section across the metal and the corrosion layer adjacent to the clay. The red line delineates the interface between the metal and the corrosion layer. The black area on the right corresponds to a resin-filled gap between the metal and the clay, which was formed during freeze-drying. The green square represents the measurement area for the  $\mu$ -Raman spectrum shown in (b). SEM, scanning electron microscopy. [Color figure can be viewed at [wileyonlinelibrary.com](http://wileyonlinelibrary.com)]



**FIGURE 2** Average corrosion rates (derived from weight loss) of corrosion coupons extracted from the IC-A experiment after 1.7 and 2.7 years.<sup>[30]</sup> [Color figure can be viewed at [wileyonlinelibrary.com](http://wileyonlinelibrary.com)]

surrounded by granular bentonite have undergone corrosion at greater corrosion rates than the ones surrounded by the block material with the same density. The estimated average corrosion rates of samples from the ABM1, ABM2 and FEBEX experiments are significantly higher (5–11 µm/a) than for the IC-A experiment, which can be explained by (i) the longer duration of oxidising conditions and (ii) the higher temperatures.

### 3.2 | Clay side

Quantitative measurements of thin bands parallel to the interface by SEM/EDX (Section 2.2) provided high-resolution elemental profiles. The Fe content (shown as Fe/Al) strongly increases toward the steel/clay interface in the ABM experiments (Figure 3). In general, the interface samples from ABM1, ABM2 and FEBEX exhibit a similar concave Fe/Al profile shape regardless of the type of the material (note that for the IC-A experiment no such analysis was carried out, but EDX analyses could identify an increased Fe content for a few 100 s of micrometres away from the metal surface, while visual observations indicated corrosion “halos” with thicknesses of 1–2 mm). The Fe front in the ABM1 and ABM2 samples extends about 5–15 mm into the clay. In some cases, there seems to be a second small front further inside the clay (Figure 3). The shape of the Fe front of the MX-80 sample from the ABM1 test, which lasted for 2.4 years, is very similar to the corresponding one of the ABM2 test, which lasted for 5.5 years. The

ABM1 sample displays only a slightly narrower front (difference of ~1 mm). This suggests a slowing down of the development of the Fe front with time. The narrowest Fe front (~4 mm) and lowest amount of transferred Fe in the ABM2 test is observed for Kunigel IV, a fine-grained bentonite. In contrast, for Ikororb located close to the Kunigel IV block, the Fe front is more extended (~10 mm).

The highly resolved Fe profiles enable an approximate estimate of the rate of corrosion-induced Fe transfer into the clay and the corrosion depths (Equation 1). The average corrosion rates derived from the EDX profiles (Table 2) for the ABM1 and ABM2 samples are several µm/a and these values are of the same order as those obtained from thickness measurements, as shown in Table 1. The total corrosion rate is thus the sum of the corrosion rates derived for the CL and the clay side of the interface in the case of the ABM1, ABM2 and FEBEX experiments (Table 2). It should be noted that the large range for the FEBEX experiment is obtained from several corrosion experiments and Fe–bentonite interaction studies, as summarised in Wersin and Kober.<sup>[23]</sup> This topic is further discussed in Section 4.

The identification of newly formed Fe-containing phases in clay is challenging because of (i) the inherent limitations of the applied analytical methods, (ii) the possibly microcrystalline nature of the precipitates (e.g., Fe hydroxides) and (iii) the mechanically disturbed contact zone with very limited amounts of the sample material.<sup>[21]</sup> In this context, <sup>57</sup>Fe Mössbauer spectrometry has proven to be a valuable tool, especially when combined with “standard” methods, such as XRF and XRD. In particular, this method enables the evaluation of the overall reduction level (Fe(II)/Fe<sub>tot</sub>) and distinguishing between different Fe(III) and Fe(II) species in clay materials.<sup>[21,25,31]</sup> An example of the Mössbauer spectra from the FEBEX sample, which is presented in Figure 4, shows the relative proportions of the main Fe species (structural Fe(III), goethite, haematite and paramagnetic Fe(II)) as a function of the distance from the Fe/clay interface. Thus, at the direct contact point, the average oxidation state of Fe increases because of the accumulation of Fe(III) oxides (mainly goethite), but in parallel paramagnetic Fe(II) (i.e., sorbed Fe(II), ferrous hydroxide or structural Fe(II) from the clay fraction) has also formed. Further away from the contact point, the share of paramagnetic Fe(II) is increased, leading to a higher reduction level relative to the unreacted bentonite. Based on the combined analytical results, structural Fe(II) and sorbed Fe(II) are the most likely species (of the paramagnetic Fe(II) fraction) to have formed as a result of interaction between the diffusing Fe(II) and the clay.<sup>[21]</sup> Similar patterns were identified for a range of

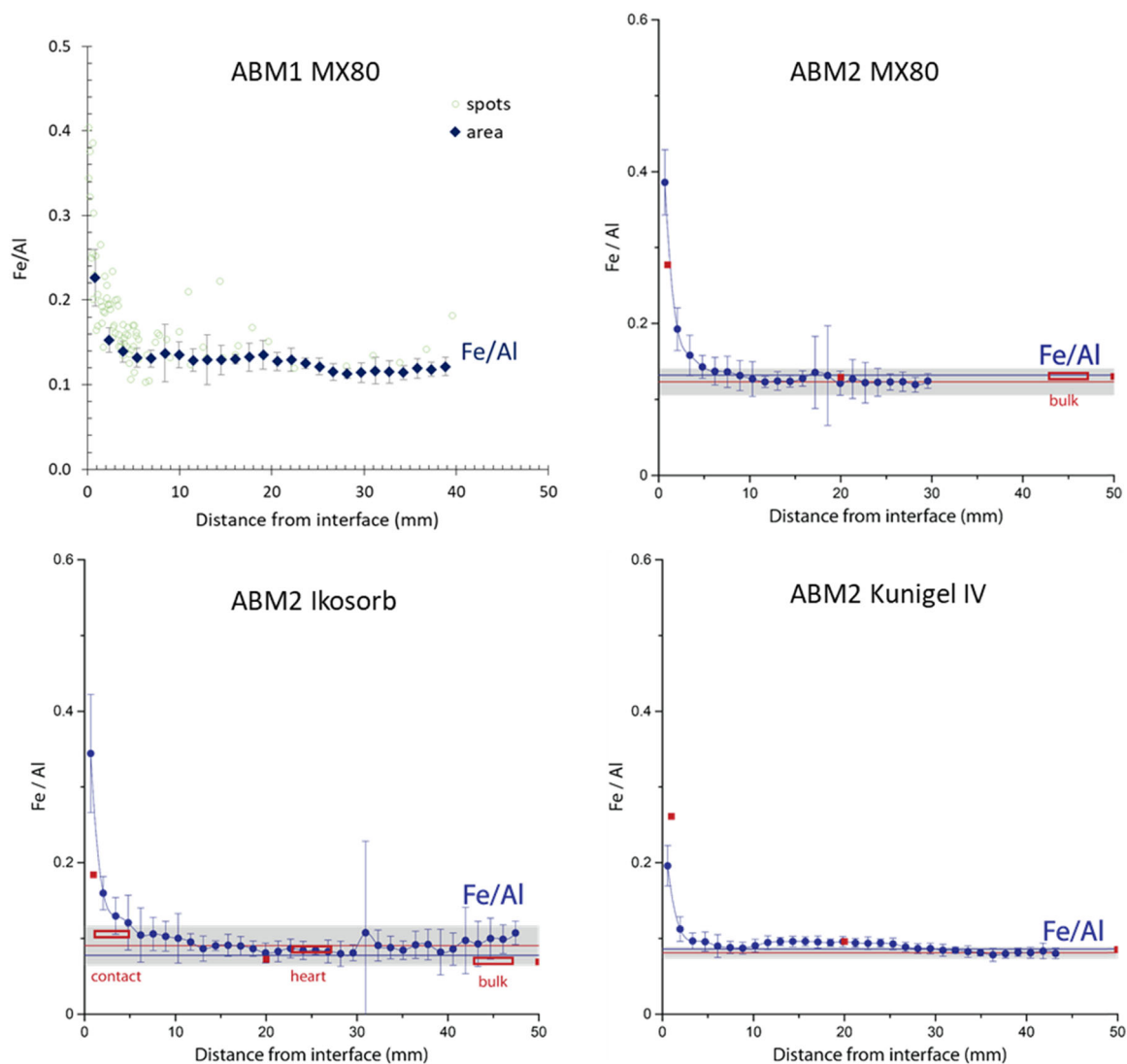


**FIGURE 3** Fe/Al ratios as a function of distance from the interface from averaged EDX maps (full symbols), EDX spot analyses (green symbols) and XRF analysis (red symbols). Error bars: range of EDX measurements at the same distance from contact. Grey area: range of bulk. Samples from ABM1 and ABM2 experiments. EDX, electron dispersive X-ray analysis; XRF, X-ray fluorescence. [Color figure can be viewed at [wileyonlinelibrary.com](https://onlinelibrary.wiley.com/terms-and-conditions)]

different bentonite materials in the ABM2 experiment.<sup>[21]</sup> The distribution of iron species in the interface area for one of the FEBEX samples, which exhibited a particularly large Fe front of >50 mm, is illustrated in Figure 5. Thus, the additional Fe at the contact point consists mainly of goethite, but further out, it is dominated by Fe(II), although at much lower total Fe levels.

## 4 | DISCUSSION

### 4.1 | Conceptual model

The analysis of interface samples from long-term in situ corrosion experiments for a range of different carbon

steels and bentonite materials, experimental designs and environmental settings reveals systematic patterns and allows conceptualisation of the corrosion and Fe–clay interaction processes in terms of the redox evolution of the repository system.<sup>[20,25]</sup> Initially, the system is oxidising and the metal surface (covered by a thin magnetite or Fe(III) oxide film) is in contact with a partially saturated bentonite containing predominantly Fe(III) phases (structural Fe and Fe(III) oxides). The evolution of the system can be separated into three distinct phases (Figure 6), as follows:

*Phase 1:* Aerobic corrosion of steel occurs, leading to the precipitation of Fe oxides at the metal/clay interface. Bentonite does not interact with the corrosion products due to their low solubility and limited water activity but

TABLE 2 Conditions and results of clay side analysis of interface samples.

Exp.	Max. temperature (°C)	Duration (year)	Fe products in clay	Redox conditions	Avg. corr. rate clay (µm/a)	Avg. corr. rate total	Ref.
IC-A	14	1.7	Fe(III) ox <sup>a</sup>	"Anaerobic"	n.d.	1.4–3.4 <sup>c</sup>	[26]
	14	2.8	Fe(III) ox <sup>a</sup>	"Anaerobic"	n.d.	0.9–2.1 <sup>c</sup>	[27]
FEBEX	70	18	goe, Fe(II) <sub>str</sub> , mah	Mixed	0–14 <sup>a,b</sup>	6–25 <sup>d</sup>	[25]
ABM1	115	2.4	goe, lep, sid, mag	Mixed	5–8 <sup>a</sup>	10–16 <sup>d</sup>	[18]
ABM2	130	5.5	goe, mag?, Fe(II) <sub>str</sub>	Mixed	4–6 <sup>a</sup>	n.d.	[19–21]

Note: Blue font: Fe(III) oxides, green font: Fe(II) bearing phases.

Abbreviations: Fe(II)<sub>str</sub>, structural Fe(II); goe, goethite; lep, lepidocrocite; mag, magnetite; mah, maghemite; max., maximum; n.d., not determined; sid, siderite.

<sup>a</sup>Estimated according to second term in Equation (1).

<sup>b</sup>Range reflects two samples from two different blocks (see Section 2.1).

<sup>c</sup>Determined from weight loss measurements.

<sup>d</sup>Estimated from Equation (1).

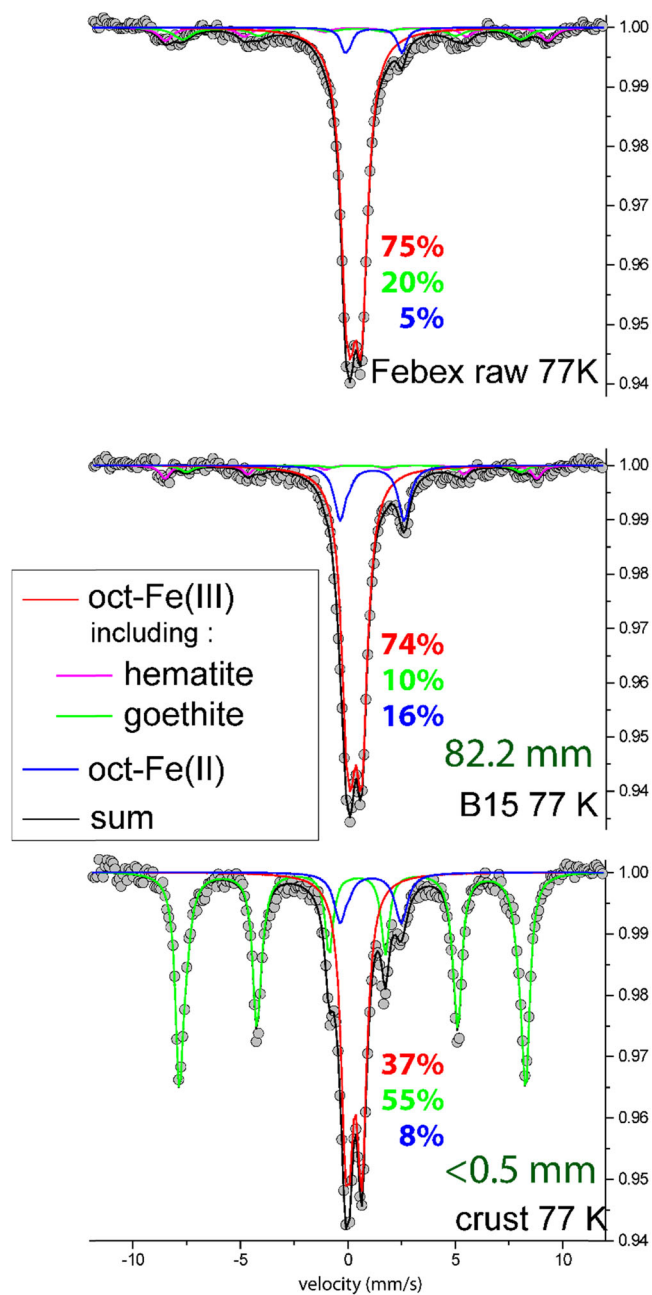
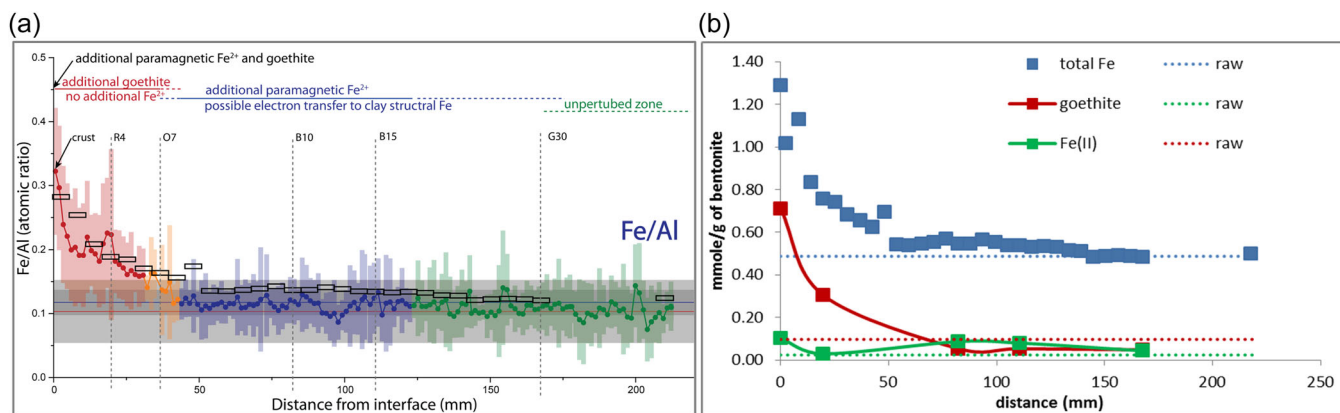


FIGURE 4 Room-temperature Mössbauer spectra of raw and reacted subsamples from two different distances from the steel/clay interface of block BM-B-41-1(Section 62) of the FEBEX experiment. Oct-Fe(II), octahedral Fe(II); Oct-Fe(III), octahedral Fe(III). [Color figure can be viewed at [wileyonlinelibrary.com](http://wileyonlinelibrary.com)]

provides the ingredients ( $O_2$  and  $H_2O$ ) for the corrosion reaction. The oxygen and  $H_2O$  flux to the metal diminishes as the CL thickens.

*Phase 2:* Anaerobic corrosion becomes dominant leading to the release of hydrogen and Fe(II), the precipitation of magnetite and, depending on the pore-water composition, siderite and/or other Fe(II) mineral



**FIGURE 5** (a) Analysis of the iron–bentonite interface of block BM-B-41-1(Section 62) of the FEBEX experiment: Fe/Al ratios as a function of distance from the interface, derived from averaged EDX maps (full symbols) and XRF (open rectangles). The shaded red blue and green areas reflect the range of EDX measurements at the same distance from the contact. Colours are assigned based on the visual appearance of powdered samples. Grey area: standard deviation ( $2\sigma$ ) of bulk. Vertical grey lines: samples analysed by Mössbauer spectrometry and XRD. (b) Fe profiles showing total concentrations and concentrations of goethite and Fe(II) (modified from Hadi et al.<sup>[25]</sup>). EDX, electron dispersive X-ray analysis; XRD, X-ray diffraction; XRF, X-ray fluorescence. [Color figure can be viewed at [wileyonlinelibrary.com](http://wileyonlinelibrary.com)]

phases. Furthermore, Fe(II) is generated at the interface via electron transfer through the CL<sup>[32,33]</sup> and reacts with the remaining O<sub>2</sub> in the bentonite, leading to Fe(III) oxide precipitation. The accumulation of Fe(III) oxides may affect the mechanical properties of the swelling bentonite as indicated by the formation of preferential cracks at the interface during sample treatment (Figure 7a) or even by “corrosion” halos formed in voids of the granular bentonite, which provide pathways for further Fe(II) transport (Figure 7b).

**Phase 3:** After depletion of O<sub>2</sub>, anaerobic corrosion proceeds with a slow further build-up of the CL and simultaneous release of Fe(II) into the clay. The Fe(II) diffuses into, and interacts with, the clay while being attenuated. This complex process probably involves a redox reaction with structural Fe(III) leading to an increase of sorbed Fe(II) and/or structural Fe(II)<sup>[12,25]</sup> but the precise mechanism is still not clear at this stage. Figure 6 illustrates a simplified scheme of the proposed conceptual model.

This conceptual model was developed based on observations from the two ABM and the FEBEX experiments, all of which were emplaced under oxidising and unsaturated conditions with residual air in the bentonite pores. Thus, the studied steel–bentonite system was exposed (under a thermal gradient) to oxidising conditions at first (Phase 1) and shifted to reducing conditions (Phases 2 and 3) during the course of the experiment. The attainment of Phase 3 is indicated by the occurrence of an Fe(II) front well beyond the CL, but the precise time evolution is not known. Observed

corrosion features suggest that Phases 1 and 2 were strongly accentuated in FEBEX compared to ABM1 and ABM2, presumably because of the influx of O<sub>2</sub> via a leak through the cement plug and the effects caused by the first excavation/dismantling phase. Regarding the IC-A experiment, initial conditions were different, because anaerobically presaturated bentonite modules containing carbon steel coupons were emplaced into a vertical Ar-filled borehole. Thus, it can be expected that only traces of oxygen were available initially and that this oxidant would be rapidly consumed. Nevertheless, the formation of Fe(III) oxides in the bentonite occurred for an extended time period while corrosion rates were low (but decreasing with time). This indicates a prolonged Phase 2 period, involving anaerobic corrosion of the metal surface surrounded by an oxidising clay. This observation was tentatively explained by proposing the presence of sorbed O<sub>2</sub> in bentonite as supported by reactive transport modelling<sup>[34]</sup> (see Section 4.2). Conversely, in the ABM and FEBEX experiments, the presence of a reduced clay zone and the occurrence of additional paramagnetic Fe(II) (as evidenced by Mössbauer spectrometry) beyond the iron oxide layer were interpreted as an indication of Fe(II) diffusion into the clay after depletion of O<sub>2</sub> in that material.<sup>[21,25]</sup> At this point, the mobility of O<sub>2</sub> and its attenuation in the bentonite remains somewhat unclear.<sup>[35,36]</sup> It should, however, be pointed out that the temperatures as well as the metal surface-to-bentonite volume ratios were much higher in the ABM and FEBEX experiments compared to the IC-A experiment. Moreover, gas transport was



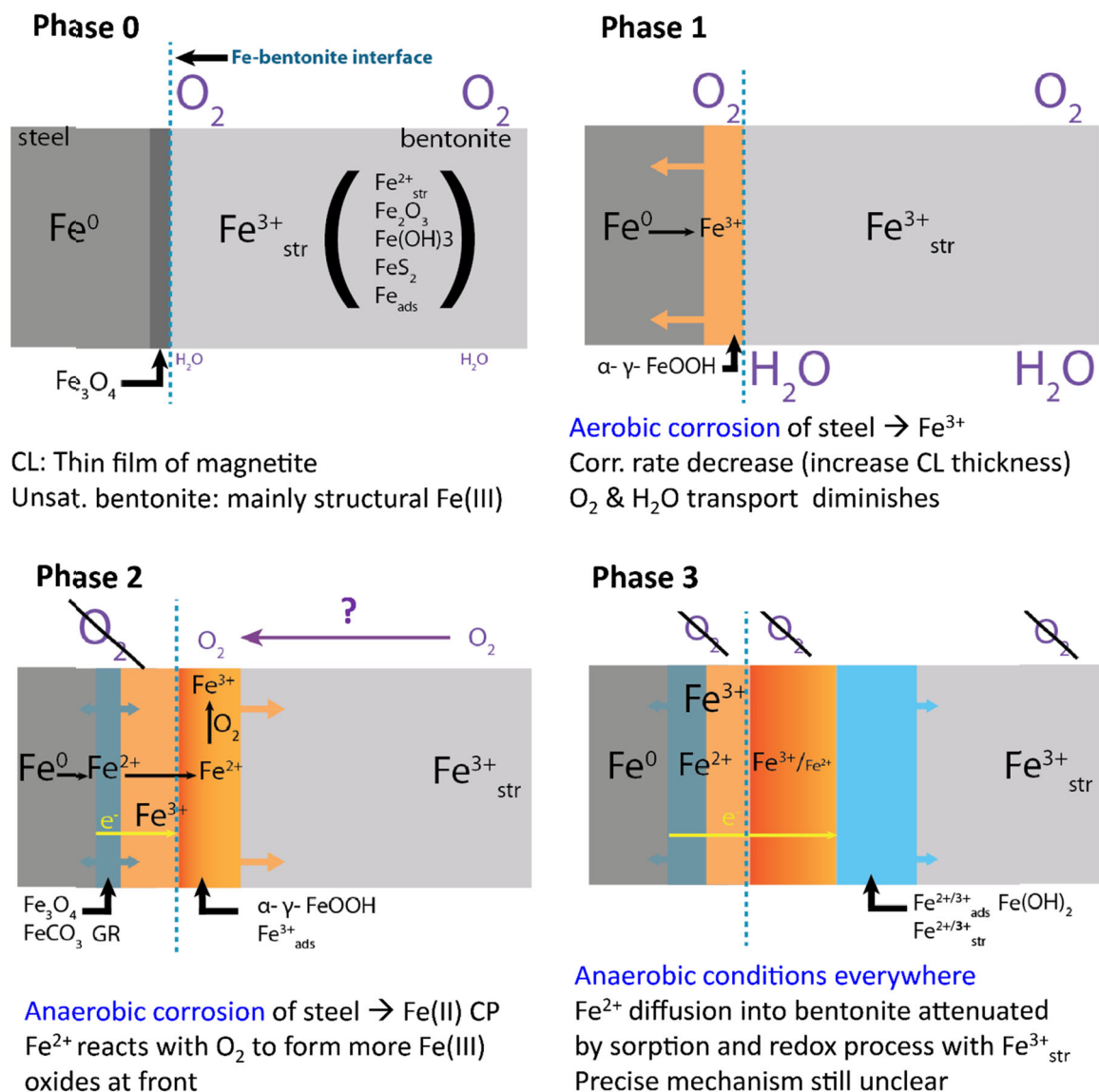


FIGURE 6 Conceptual model of corrosion and the Fe-clay interaction process based on Hadi and colleagues.<sup>[20,21,25]</sup> [Color figure can be viewed at [wileyonlinelibrary.com](https://onlinelibrary.wiley.com/terms-and-conditions)]

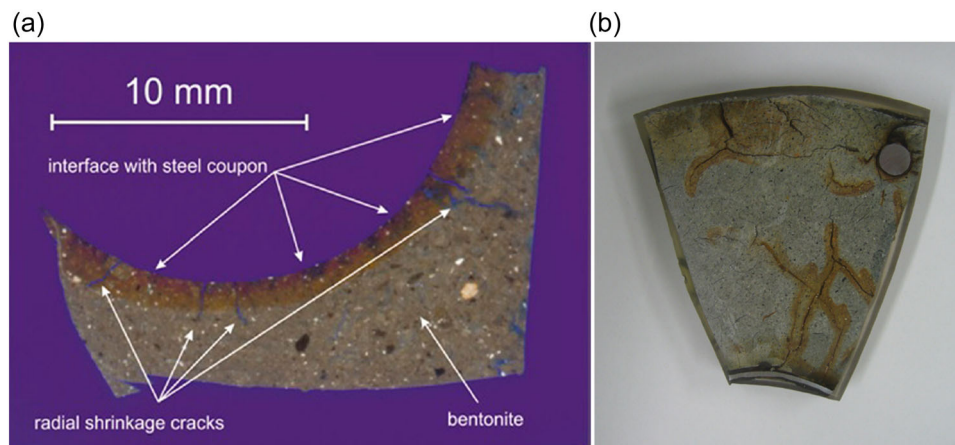
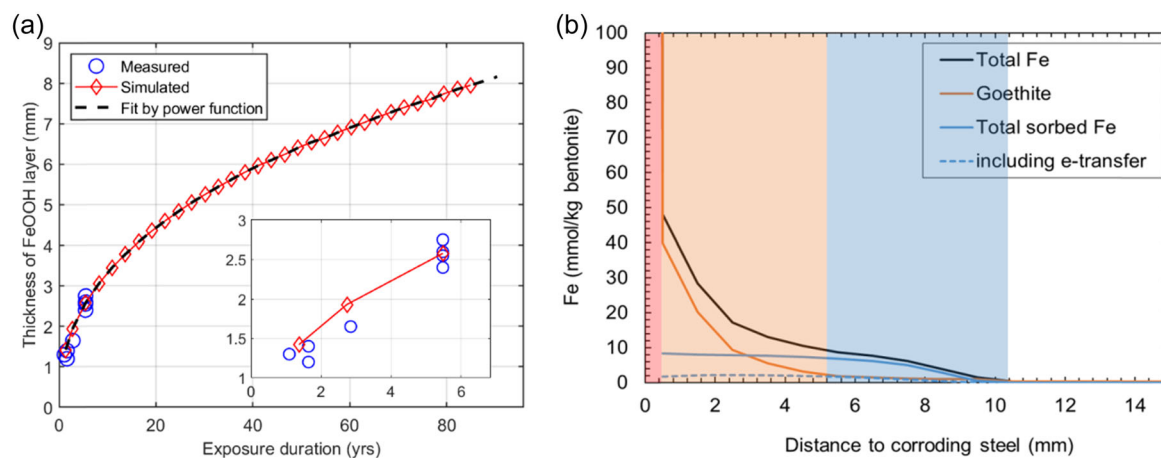


FIGURE 7 (a) Transmitted light image (blue-dye epoxy-resin impregnated sample) through the steel/bentonite interface of the IC-A experiment (BM2-4 coupon removed, Module 1,  $1450 \text{ kg m}^{-3}$ ).<sup>[26]</sup> (b) Image of the ABM2 granular bentonite sample inside the metal cage showing Fe (oxyhydr)oxide-rich areas in voids that were sealed upon saturation.<sup>[20]</sup> [Color figure can be viewed at [wileyonlinelibrary.com](https://onlinelibrary.wiley.com/terms-and-conditions)]



**FIGURE 8** (a) Simulated (diamonds) and measured (circles) FeOOH layer thicknesses around corrosion coupon versus time (IC-A experiment).<sup>[34]</sup> (b) Simulated Fe (total and different species) profiles versus distance to corroding steel.<sup>[37]</sup> Colours reflect macroscopically visible alteration zones. [Color figure can be viewed at [wileyonlinelibrary.com](http://wileyonlinelibrary.com)]

favoured in the partially saturated ABM and FEBEX experiments, whereas  $O_2$  transport in the presaturated IC-A experiment would be largely restricted to solute diffusion if it happens at all. In the case of the FEBEX experiment, the observed pronounced but heterogeneous corrosion features suggest a more prolonged Phase 2 due to additional  $O_2$  input through a leaky plug,<sup>[23]</sup> but because of the partially saturated conditions, elevated temperatures and temperature gradients,  $O_2$  mobility was greater compared to that in the IC-A experiment. To shed more light on the interaction of corrosion-derived Fe(II) with molecular  $O_2$  and the evolution of redox conditions under the specific conditions of the in situ experiments, a reactive transport model approach is required. The first examples of such modelling are provided in the following section.

## 4.2 | Modelling attempts

Reactive transport modelling can provide additional insight into the corrosion processes occurring during in situ experiments and help to elucidate the impact of different environmental parameters (e.g., temperature, moisture content). So far, however, very few attempts have been made in this direction.

One example is the modelling exercise carried out for the IC-A experiment<sup>[34]</sup> in which the corrosion process was modelled during Phase 2 (i.e., anaerobic corrosion, oxic bentonite) using a one-dimensional diffusion–precipitation approach to simulate the evolution of Fe(II) and Fe(III) profiles from the metal surface into the bentonite (Figure 8a) with time. The model considered time-dependent corrosion based on experimentally derived corrosion rate data,<sup>[38]</sup>

diffusion of Fe(II) into the clay coupled with kinetic oxidation to Fe(III) and precipitation of  $\alpha$ -FeOOH (goethite). Furthermore, the model assumed  $O_2$  in the clay to be immobile. The simulated FeOOH thickness was in agreement with the measured thicknesses over the course of the experiment and could be fitted with a simple power function (Figure 8a).

Another example of modelling iron–bentonite interactions is the rather complex thermo–hydrochemical (THC) model that is currently being developed for simulating the FEBEX in situ experiment within the European Joint Programme EURAD ([www.ejp-eurad.eu](http://www.ejp-eurad.eu)). It includes bentonite saturation within a thermal gradient, two-phase flow and a complete geochemical reaction network. The numerical model builds on the conceptual model of Hadi et al.<sup>[25]</sup> as summarised in Section 4.1, thus the model includes all three phases and hence the transition from aerobic to anaerobic corrosion. Preliminary results presented at the Clay Conference in Nancy (June 2022)<sup>[37]</sup> indicate that the observed concave shape of the Fe front and the corrosion patterns can be adequately simulated (Figure 8b), although the large extension of the observed alteration zones of the FEBEX sample described above was not well matched with the current version of the THC model.

## 5 | CONCLUSIONS

The careful microscopic and spectroscopic analyses of steel/bentonite interface samples removed from four in situ test settings provided valuable information about the corrosion processes occurring during the early stages of an

high level waste repository after its closure. Systematic patterns could be deduced irrespective of carbon steel grade, type of bentonite and its degree of compaction, geochemical environment or experiment setup. Thus, a clear dependence of the corrosion rates on temperature and reaction time as well as on the availability of H<sub>2</sub>O and O<sub>2</sub> provided by the surrounding bentonite buffer was indicated. A further important and potentially safety-relevant feature is the reaction of corrosion-derived Fe(II) with structural Fe(III) in the clay. Recent developments highlight the usefulness of reactive transport modelling in understanding the coupled corrosion and Fe–clay interaction processes.

Two important remaining uncertainties are the mobility of O<sub>2</sub> in the bentonite and the diffusion and attenuation of Fe(II) in the bentonite under reducing conditions. The latter process is currently under investigation within the European EURAD programme.

### AUTHOR CONTRIBUTIONS

Paul Wersin was involved in conceptualisation, investigation, writing—original draft, review and editing and project management. Jebril Hadi, Mirjam Kiczka, Andreas Jenni, Jean-Marc Grenèche, Bharti Reddy, Nicholas Smart and Zhidong Zhang were involved in the investigation, writing—original draft and editing. Nikitas Diomidis, Olivier X. Leupin were involved in conceptualisation and writing—original draft and editing. Daniel Svensson and Patrik Sellin were involved in conceptualisation.

### ACKNOWLEDGEMENTS

The authors would like to acknowledge Urs Mäder, Margarita Koroleva and Samuel Gilgen for their help with sampling and laboratory work and the team of the polishing workshop for their cautious preparation of the polished surfaces (Institute of Geological Sciences, University of Bern). The authors would also thank Stephan Kaufhold and Reiner Dohrmann from BGR (Germany) for providing the large X-ray fluorescence data set on the ABM samples. The entire multinational team involved in ABM and FEBEX is acknowledged for fruitful discussions and the authors are grateful to all the members of the corrosion research team at Jacobs and the supporting analysts at Oxford University and BGS. The study was financially supported by Nagra (Switzerland), SKB (Sweden) and EURAD. Open access funding provided by Universitat Bern.

### CONFLICT OF INTEREST STATEMENT

The authors declare no conflict of interest.

### DATA AVAILABILITY STATEMENT

The data that support the findings of this study are available from the corresponding author upon reasonable request.

### ORCID

Paul Wersin  <http://orcid.org/0000-0003-4359-6695>

Nikitas Diomidis  <http://orcid.org/0000-0002-3875-2633>

Bharti Reddy  <http://orcid.org/0000-0003-0011-0296>

Nicholas Smart  <http://orcid.org/0000-0001-8577-5937>

### REFERENCES

- [1] M. I. Ojovan, H. J. Steinmetz, *Energies* **2022**, *15*, 7804.
- [2] D. Andra, *Andra report C.RP.ASCM.04.0015.A*, Châtenay-Malabry, France, **2005**.
- [3] R. Patel, C. Punshon, J. Nicholas, P. Bastid, R. Zhou, C. Schneider, N. Bagshaw, D. Howse, E. Hutchinson, R. Asano, *Nagra Technical Report NTB 12-06*, Wetingen, Switzerland, **2012**.
- [4] I. Pospiskova, D. Dobrev, M. Kouril, J. Stoullil, D. Novikova, P. Kotnour, O. Matal, *Corros. Eng., Sci. Technol.* **2017**, *52*, 6.
- [5] SKB, *SKB Technical Report TR-11-01*, Stockholm, Sweden, **2011**.
- [6] Posiva, *Report POSIVA 2012-03*, Olkiluoto, Finland, **2012**.
- [7] P. Wersin, L. H. Johnson, B. Schwyn, U. Berner, E. Curti, *Nagra Technical Report NTB 02-13*, Nagra, Wetingen, Switzerland, **2003**.
- [8] O. Leupin, P. Smith, P. Marschall, L. Johnson, D. Savage, V. Cloet, J. Schneider, *Nagra Technical Report NTB 14-13*, Wetingen, Switzerland, **2016**.
- [9] F. King, *F. Nagra Technical Report NTB 08-12*, Wetingen, Switzerland, **2008**.
- [10] A. Muurinen, A. C. Tournassat, J. Hadi, J.-M. Grenèche, *Posiva Working Report 2014-04*, Olkiluoto, Finland, **2014**.
- [11] L. Carlson, O. Karnland, V. M. Oversby, A. P. Rance, N. R. Smart, M. Snellman, M. Vähänen, L. O. Werme, *Phys. Chem. Earth* **2007**, *32*, 334.
- [12] D. E. Latta, A. Neumann, W. A. P. J. Premaratne, M. M. Scherer, *ACS Earth Space Chem.* **2017**, *1*, 197.
- [13] J. Hadi, C. Tournassat, I. Ignatiadis, J.-M. Grenèche, L. Charlet, *J. Colloid Interface Sci.* **2013**, *407*, 397.
- [14] P. Wersin, M. Birgersson, S. Olsson, O. Karnland, *Report POSIVA -11*, Olkiluoto, Finland, **2007**.
- [15] N. Diomidis, F. King, Nuclear Corrosion, Elsevier, **2020**, p. 371.
- [16] A. Eng, U. Nilsson, D. Svensson, *SKB International Progress Report IPR-07-15*, Stockholm, Sweden, **2007**.
- [17] D. Svensson, A. Dueck, U. Nilsson, S. Olsson, T. Sandén, S. Lydmar, S. Jägerwall, K. Pedersen, S. Hansen, *SKB Technical Report TR-11-06*, Stockholm, Sweden, **2011**.
- [18] P. Wersin, A. Jenni, U. K. Mäder, *Clays Clay Miner.* **2015**, *63*, 51.
- [19] S. Kaufhold, R. Dohrmann, N. Götze, D. Svensson, *Clays Clay Miner.* **2017**, *65*, 27.
- [20] J. Hadi, P. Wersin, A. Jenni, J.-M. Grenèche, *Nagra Technical Report NTB 2017-10*, Wetingen, Switzerland, **2017**.
- [21] P. Wersin, J. Hadi, A. Jenni, D. Svensson, J.-M. Grenèche, P. Sellin, O. X. Leupin, *Minerals* **2021**, *11*, 907.
- [22] A. M. Fernández, N. Giroud, *Nagra Arbeitsbericht NAB 16-13*, Wetingen, Switzerland, **2017**.
- [23] P. Wersin, F. Kober, *Nagra Arbeitsbericht NAB 16-16*, Wetingen, Switzerland, **2017**.
- [24] F. Kober, J. L. García-Siñeriz, M. V. Villar, G. W. Lanyon, V. Cloet, U. Mäder, P. Wersin, O. X. Leupin, P. Sellin, A. Gens, R. Schneeberger, *Nagra Technical Report NTB 17-01*, Wetingen, Switzerland, **2021**.

- [25] J. Hadi, P. Wersin, V. Serneels, J. M. Greneche, *Clays Clay Miner.* **2019**, *67*, 111.
- [26] N. R. Smart, B. Reddy, A. P. Rance, D. J. Nixon, M. Frutschi, R. Bernier-Latmani, N. Diomidis, *Corros. Eng., Sci. Technol.* **2017**, *52*, 101.
- [27] B. Redd, C. Padovani, N. R. Smart, A. P. Rance, A. Cook, A. Milodowski, L. Field, S. Kemp, N. Diomidis, *Mater. Corros.* **2021**, *72*, 268.
- [28] ASTM, Standard practice for preparing, cleaning, and evaluating corrosion test specimens, G1, ASTM, Philadelphia, PA, USA. **2011**.
- [29] D. Féron, D. Crusset, J.-M. Gras, *J. Nucl. Mater.* **2008**, *379*, 16.
- [30] N. Diomidis, V. Deydier, M. Jendras, F. Heberling, J. Binns, M. Cowley, B. Reddy, R. Bernier-Latmani, presented at Mont Terri Techn. Meeting, St. Ursanne, Switzerland, January 2022.
- [31] L. Charlet, C. Tournassat, J.-M. Grenèche, P. Wersin, A. Géhin, J. Hadi, *J. Mater. Res.* **2022**, *1*, 1.
- [32] K. M. Rosso, S. V. Yanina, C. A. Gorski, P. Laresse-Casanova, M. M. Scherer, *Environ. Sci. Technol.* **2010**, *44*, 61.
- [33] R. M. Handler, A. J. Friedrich, C. M. Johnson, K. M. Rosso, B. L. Beard, C. Wang, D. E. Latta, A. Neumann, T. Pasakarnis, W. A. P. J. Premaratne, M. M. Scherer, *Environ. Sci. Technol.* **2014**, *48*, 11302.
- [34] O. X. Leupin, N. R. Smart, Z. Zhang, M. Stefanoni, U. Angst, A. Papafotiou, N. Diomidis, *Corr. Sci.* **2021**, 109523.
- [35] N. Giroud, Y. Tomonaga, P. Wersin, S. Briggs, F. King, T. Vogt, N. Diomidis, *Appl. Geochem.* **2018**, *97*, 270.
- [36] Y. Tomonaga, P. Wersin, D. Rufer, P. Koho, V. Heino, R. Kipfer, *Appl. Geochem.* **2021**, *138*, 105205.
- [37] M. Kiczka, P. Wersin, P. Alt-Epping, J. Hadi, O. Leupin, N. Diomidis, presented at 8th Clay Conf., Radioac. Waste Confinement, Nancy, France, June 2022.
- [38] N. Diomidis, B. Reddy, *Nagra Arbeitsbericht NAB 20-010*, Wettingen, Switzerland, **2022**.
- [39] M. Bradbury, U. Berner, E. Curti, W. Hummel, G. Kosakowski, T. Thoenen, *Nagra Technical Report NTB 12-01*, Wettingen, Switzerland, **2014**.

**How to cite this article:** P. Wersin, J. Hadi, M. Kiczka, A. Jenni, J.-M. Grenèche, N. Diomidis, O. X. Leupin, D. Svensson, P. Sellin, B. Reddy, N. Smart, Z. Zhang, *Mater. Corros.* **2023**, 1–12.  
<https://doi.org/10.1002/maco.202313755>